

1 **Transport by Lagrangian Vortices in the Eastern Pacific**

2 Ryan Abernathey*

3 *Columbia University, New York, New York, USA*

4 George Haller

5 *ETH, Zürich, Switzerland*

6 *Corresponding author address: Ryan Abernathey, Lamont Doherty Earth Observatory of
7 Columbia University, 205C Oceanography, 61 Route 9W - PO Box 1000, Palisades, NY 10964-
8 8000, US.

9 E-mail: rpa@ldeo.columbia.edu

ABSTRACT

10 Rotationally coherent Lagrangian vortices (RCLVs) are identified from
11 satellite-derived surface geostrophic velocities in the Eastern Pacific (180° -
12 130° W) using the objective (frame-invariant) finite-time Lagrangian-
13 coherent-structure detection method of Haller et al. (2016) based on the
14 Lagrangian-averaged vorticity deviation. RCLVs are identified for 30, 90,
15 and 270 day intervals over the entire satellite dataset, beginning in 1993. In
16 contrast to structures identified using Eulerian eddy-tracking methods, the
17 RCLVs maintain material coherence over the specified time intervals, mak-
18 ing them suitable for material transport estimates. Statistics of RCLVs are
19 compared to statistics of eddies identified from sea-surface height (SSH) by
20 Chelton et al. 2011. RCLVs and SSH eddies are found to propagate westward
21 at similar speeds at each latitude, consistent with the Rossby wave dispersion
22 relation. However, RCLVs are uniformly smaller and shorter-lived than SSH
23 eddies. A coherent eddy diffusivity is derived to quantify the contribution of
24 RCLVs to meridional transport; it is found that RCLVs contribute less than 1%
25 to net meridional dispersion and diffusion in this sector, implying that eddy
26 transport of tracers is mostly due to incoherent motions, such as swirling and
27 filamentation outside of the eddy cores, rather than coherent meridional trans-
28 lation of eddies themselves. These findings call into question prior estimates
29 of coherent eddy transport based on Eulerian eddy identification methods.

³⁰ **1. Introduction**

³¹ The mesoscale (broadly 10 - 500 km) is the most energetic scale in the ocean (Wortham and
³² Wunsch 2014). Phenomenologically, the mesoscale comprises a disorderly jumble of waves, vor-
³³ tices, fronts, and filaments, and the word mesoscale frequently appears together with the word
³⁴ “eddy.” However, a survey of the literature reveals a wide range of definitions of “eddy,” which is
³⁵ used as both an adjective and a noun. The standard Eulerian statistical perspective defines “eddy”
³⁶ (an adjective) simply as a fluctuation about an Eulerian time and / or spatial mean state. The
³⁷ coherent structure perspective attempts to identify specific, discrete “eddies” (a noun) and track
³⁸ them through the ocean. Here we seek to clarify the relationship between Eulerian eddy fluxes and
³⁹ coherent structures.

⁴⁰ Eulerian mesoscale eddy fluxes (i.e. statistical correlations between velocity and tracer fluctua-
⁴¹ tions, a.k.a. Reynolds fluxes) play a significant role in the transport of heat, salt, momentum and
⁴² other tracers through the ocean. Because climate models generally do not resolve the mesoscale,
⁴³ the sub-gridscale mesoscale flux must be parameterized based on the large-scale flow proper-
⁴⁴ ties, commonly using a diffusive closure (Gent et al. 1995; Treguier et al. 1997; Visbeck et al.
⁴⁵ 1997; Vollmer and Eden 2013; Bachman and Fox-Kemper 2013). This important problem has
⁴⁶ motivated many studies of Eulerian eddy fluxes (and associated diffusivities) in observations and
⁴⁷ eddy-resolving models (e.g. Morrow et al. 1992; Stammer 1998; Roemmich and Gilson 2001;
⁴⁸ Jayne and Marotzke 2002; Volkov et al. 2008; Fox-Kemper et al. 2012; Abernathey and Marshall
⁴⁹ 2013; Klocker and Abernathey 2014; Abernathey and Wortham 2015). This body of work has
⁵⁰ been largely unconcerned with coherent structures, although Abernathey and Wortham (2015) did
⁵¹ note the overlap between eddy flux spectral characteristics and the lengths scales and propagation
⁵² speeds of coherent mesoscale eddies.

Many different methods have been used to identify coherent structures (CSs). These methods fall into two general categories: Eulerian¹ (based on instantaneous features of the velocity field) and Lagrangian (based on time-dependent water parcel trajectories). Early Eulerian approaches used contours of the Okubo-Weiss parameter (Okubo 1970; Weiss 1991) to identify the boundaries of eddies (Isern-Fontanet et al. 2003, 2004). More recently, closed contours of the sea-surface height anomaly (SSH) field have been employed (Chelton et al. 2011, henceforth CSS11). The eddy census of CSS11 has been widely adopted by the community, likely due to its open publication on the web. Other recent Eulerian CS eddy census products include Dong et al. (2011) and Faghmous et al. (2015). While these methods differ in certain details, they are all fundamentally similar in that they use the instantaneous velocity field (or streamfunction) to identify eddies at each snapshot in time, and then track these features from one snapshot to the next.

This Eulerian approach to eddy tracking, however, suffers from several shortcomings (see Haller 2015; Peacock et al. 2015, for a discussion). Firstly, the structures identified in this way are not material; the Eulerian tracking algorithms associate spatially proximal features identified at neighbouring time snapshots with the a single object, but these features don't necessarily represent the same fluid. Secondly, the structures are not objective; different observers in frames translating and rotating relative to each other will identify different flow regions as coherent. This creates a conceptual problem because material transport by eddies should be independent of the observer, as required by basic axioms of continuum mechanics. A related issue is that OW and SSH eddies depend on arbitrary parameters or thresholds, which are routinely tuned to match expectations derived form the same methods. Finally, and most importantly from the perspective of transport, OW and SSHA eddies are *materially incoherent* to a significant extent; under Lagrangian advection, the supposed eddy boundaries become rapidly strained and filamented, implying that water leaks

¹An Eulerian method for identifying coherent structures should not be confused with the Eulerian eddy flux.

76 significantly across the structure boundaries inferred by the OW and SSH criteria (Beron-Vera
77 et al. 2013; Haller and Beron-Vera 2013).

78 Contradictions may therefore arise when such Eulerian eddy tracking methods are applied to
79 infer material transport, as in two recent studies. Dong et al. (2014) used Eulerian eddy tracking,
80 together with vertical structure functions of potential temperature and salinity derived statistically
81 from ARGO profiles, to estimate the heat and salt content materially trapped inside the eddies.
82 By assuming no exchange with the surrounding environment for the duration of the eddy lifetime,
83 they estimated the meridional fluxes of heat and salt on a global scale, reaching the conclusion
84 that "...eddy heat and salt transports are mainly due to individual eddy movements." Zhang et al.
85 (2014) used a similar method to estimate the eddy mass flux. They employed tracked Eulerian
86 eddies together with vertical structure functions to estimate the potential vorticity field surround-
87 ing the eddies. The outermost closed potential vorticity contour was assumed to constitute an
88 impermeable material boundary for the duration of each tracked eddy, and the eddy motion was
89 thereby translated to a mass flux. This method estimated the westward zonal eddy mass flux in the
90 subtropical gyre regions to be approx. 30 Sv, a surprisingly large number which is comparable to
91 the gyre transport itself. These approaches might seem quite appealing because they reduce the
92 expensive problem of observing the turbulent ocean at high spatial and temporal frequency to the
93 more tractable one of identifying and tracking a finite number of coherent eddies. However, the
94 work of Beron-Vera et al. (2013), Haller and Beron-Vera (2013), and Wang et al. (2015) provides
95 evidence that these methods strongly overestimate the degree of material coherence in mesoscale
96 eddies, calling into question the findings.

97 The goal of the present study is to make a more accurate estimate of material transport due to
98 ocean mesoscale eddies using an objective (i.e. frame independent) Lagrangian eddy detection
99 method applied to surface velocity fields derived from satellite altimetry. We focus on a sector in

the East Pacific which has been the setting for a number of studies on Eulerian eddy fluxes (Roemich and Gilson 2001; Abernathey and Marshall 2013; Klocker and Abernathey 2014; Abernathey and Wortham 2015). We apply the recently introduced Rotationally Coherent Lagrangian Vortex (RCLV) methodology based on a dynamic polar decomposition of the deformation gradient developed by (Haller 2016). The key difference between our approach and Eulerian eddy detection methods is that, by numerically advecting a dense mesh of millions of Lagrangian particles, we demonstrate (rather than assume) that our identified vortices actually remain materially coherent throughout a finite time interval, as guaranteed by their mathematical construction. Furthermore, the full Lagrangian trajectories also allow us to estimate a more broadly-defined material eddy flux due to the entire range of turbulent motions in the flow. By comparing this full flux with the transport due to the coherent vortices, we obtain an estimate of the relative importance of material transport by coherent structures to the full turbulent transport. We consider the two-dimensional surface geostrophic flow as observed by satellite altimetry, as this is the only large-scale velocity observation which resolves mesoscale structures, which limits our ability to probe subsurface transport. Nevertheless, the results strongly support the conclusion that RCLVs make only a minimal contribution to meridional eddy transport.

The paper is organized as follows. In Sec. 2, we review the RCLV definition and the concepts of Lagrangian dispersion and diffusivity. In Sec. 3, we describe the satellite data and the numerical approach to Lagrangian particle advection. Sec. 4 provides some case studies of Lagrangian vortices identified by our algorithm and summarizes their statistics. In Sec. 5, we present the eddy diffusivity and the coherent eddy diffusivity. Sec. 6 contains discussion and conclusions.

121 **2. Theory of Lagrangian Transport and Rotationally Coherent Vortices**

122 *a. Eulerian Eddy Flux and Lagrangian Diffusivity*

123 Consider a conserved two-dimensional scalar $c(x, y)$ advected by a two-dimensional velocity
124 field $\mathbf{u}(x, y, t)$ where $\mathbf{u} = (u, v)$. The time- and zonal-mean meridional flux of the scalar across a
125 latitude circle in a sector of the ocean is given by \overline{vc} . The overbar represents the time and zonal
126 average:

$$\overline{vc} = (L_x T)^{-1} \int_{x_0}^{x_0 + L_x} \int_{t_0}^{t_0 + T} vc dx , \quad (1)$$

127 where L_x is the zonal extent of the sector and T is the averaging time period. We observe that \overline{vc} ,
128 as any scalar flux across a designated surface, is objective, i.e. independent of the observer. To
129 capture the contribution of eddies to the mean meridional flux accurately, one therefore needs an
130 observer-independent eddy-identification scheme.

131 The Lagrangian dynamics of the flow are described by the kinematic equation

$$\frac{\partial \mathbf{X}}{\partial t} = \mathbf{u} , \quad (2)$$

132 where $\mathbf{X} = (X, Y)$ is the position vector. We denote the initial fluid parcel positions at $t = 0$
133 as $\mathbf{x}_0 = (x_0, y_0)$. We can use this initial position to label the fluid parcels at a later time: $\mathbf{X} =$
134 $\mathbf{X}(x_0, y_0, t)$. For homogeneous, statistically stationary turbulent flow, Taylor (1921) identified the
135 relationship between the Eulerian mean flux \overline{vc} and the Lagrangian statistics as

$$\overline{vc} = -K_{abs} \frac{\partial \overline{c}}{\partial y} \quad (3)$$

136 with

$$K_{abs} = \frac{1}{2} \frac{\partial}{\partial t} \overline{Y^2} . \quad (4)$$

137 Here $\overline{Y^2}$ represents the mean squared Lagrangian displacement of water parcels from their initial
138 position, i.e. absolute dispersion; K , the growth rate of this absolute dispersion, represents the

139 single particle or absolute diffusivity (LaCasce 2008). Regardless of whether the flow statistics
 140 are truly diffusive or not, eqs. (3) and (4) represent the kinematic relationship between Lagrangian
 141 displacement and Eulerian flux. The diffusivity K_{abs} expresses the fundamental transport proper-
 142 ties of the flow, independently of the background gradient $\partial \bar{c} / \partial y$. Note that K_{abs} is an objective
 143 quantity by (3), since both $\bar{v}c$ and $\partial \bar{c} / \partial y$ are objective. (The frame-independence of $\partial \bar{c} / \partial y$ can be
 144 seen by noting that it is the directional derivative of \bar{c} along the normal of a latitude circle.) Equiv-
 145 alently, (4) is objective, since the displacement Y is defined relative the the reference latitude.

146 From an Eulerian perspective, the eddy component of the flux is readily identified via a standard
 147 Eulerian Reynolds decomposition: $\bar{v}c = \bar{v}c + \bar{v}'c'$, where the prime indicates the instantaneous
 148 deviation from the Eulerian mean. The second term $\bar{v}'c'$ is commonly termed the eddy flux. Taylor
 149 envisioned a homogeneous, isotropic turbulent flow with no mean component, i.e. $\bar{v} = 0$, such
 150 that $\bar{v}c = \bar{v}'c'$. In contrast, most geophysical flows have mean flows, and the mean advection can
 151 influence K_{abs} . One way to remove the effects of the mean flow in the Lagrangian frame is to
 152 instead focus on the relative diffusivity (Batchelor 1952; Bennett 1984)

$$K_{rel} = \frac{1}{2} \frac{\partial}{\partial t} \overline{(Y - \bar{Y})^2}, \quad (5)$$

153 which represents the growth rate of the second moment of the ensemble displacement. In this
 154 case, the ensemble consists of all water parcels originating at a particular latitude. (Relative dif-
 155 fusivity can equivalently be calculated from pair separation statistics [LaCasce 2008].) A detailed
 156 discussion of the relationship between K_{abs} , K_{rel} , and the mixing of a passive tracer is given by
 157 Klocker et al. (2012). For the purposes of this study, we shall take K_{rel} to be the most relevant
 158 diagnostic of net meridional eddy transport in our sector. Our goal is to identify the contribution
 159 of coherent Lagrangian eddies to K_{rel} . Like K_{abs} , K_{rel} is an objective quantity. As noted above, a

₁₆₀ self-consistent and accurate assessment of the coherent-eddy component K_{rel} should also be based
₁₆₁ on objective eddy identification schemes, such as the one described next.

₁₆₂ *b. Rotationally Coherent Lagrangian Vortices*

₁₆₃ In order to partition the transport defined in (4) and (5) into a contribution from coherent La-
₁₆₄ grangian eddies, the domain must be divided into regions inside and outside a suitably defined
₁₆₅ eddy boundary. For the boundary to be relevant for transport, it must be a material line (in 2D)
₁₆₆ or surface (in 3D) derived from an objective (frame-invariant) method. The identification of such
₁₆₇ boundaries in unsteady turbulent flows is the subject of much recent work from the field of dynam-
₁₆₈ ical systems, and several possible criteria exist (for a review see Haller 2015). We emphasize again
₁₆₉ that the Eulerian eddy identification methods of CSS11 are not objective and depend on choices of
₁₇₀ thresholds and parameters. Consequently, they yield boundaries which, when advected as material
₁₇₁ lines, rapidly deform and disperse away from the supposed eddy center (Beron-Vera et al. 2013;
₁₇₂ Haller and Beron-Vera 2013).

₁₇₃ One sensible criterion is to define eddy boundaries as closed material curves which experi-
₁₇₄ ence minimal tangential stretching over a finite-time interval, so-called elliptic LCSs (Haller and
₁₇₅ Beron-Vera 2012). A more general approach locates material eddy boundaries that exhibit uni-
₁₇₆ form stretching and hence show no filamentation (Haller and Beron-Vera 2013). The elliptic LCS
₁₇₇ detection methods have been applied to study Agulhas rings (Beron-Vera et al. 2013; Haller and
₁₇₈ Beron-Vera 2013; Wang et al. 2015). The underlying variational principles guarantee perfect lack
₁₇₉ of filamentation for the boundaries and hence tend to be stringent and computationally complex.
₁₈₀ (Recent work by Serra and Haller 2017 has, however, simplified the necessary computations con-
₁₈₁ siderably.)

182 Here we opt for a fluid-mechanically more intuitive approach based on vorticity. Haller et al.
 183 (2016) showed that rotationally coherent Lagrangian vortex (RCLV) boundaries can be identified
 184 as the outermost closed contours of the Lagrangian-averaged vorticity deviation (LAVD, defined
 185 below). The physical essence of an RCLV is the notion that all fluid parcels along a coherent mate-
 186 rial vortex boundary should rotate at the same average angular velocity over a finite-time interval,
 187 in analogy to solid body rotation. The LAVD technique enables the identification of such coher-
 188 ently rotating structure boundaries from Lagrangian trajectory data. Haller et al. (2016) further
 189 showed that the RCLVs identified in this way coincided with structures identified by the earlier
 190 elliptic LCS methods, although the RCLV boundaries were larger². Given the relative computa-
 191 tional simplicity and the familiarity of vorticity to most physical oceanographers, we adopt this
 192 approach as our eddy identification technique. Here we briefly review the practical elements of
 193 the theory and refer the reader to Haller et al. (2016) for a deeper mathematical treatment.

194 The instantaneous relative vorticity in two dimensions is

$$\zeta(x,y,t) = -\frac{\partial u}{\partial y} + \frac{\partial v}{\partial x}. \quad (6)$$

195 The vorticity deviation is obtained by subtracting the spatial average, i.e. $\zeta'(x,y,t) = \zeta - \langle \zeta \rangle(t)$.
 196 (Angle brackets indicate an average over the whole computational domain.) Subtracting the mean
 197 vorticity field removes any solid body rotation of the entire domain and is required to maintain
 198 the frame invariance of the method (Haller et al. 2016). In practice, however, when the domain
 199 is the entire ocean, the mean vorticity is rather negligible. A Lagrangian-averaged quantity is
 200 the instantaneous quantity averaged along the evolving flow trajectory (as opposed to an Eulerian

²These larger boundaries are no longer guaranteed to be completely free from filamentation under material advection. However, by construction, any filamentation they might exhibit is tangential to the boundary, and hence the stretched boundary keeps traveling with the eddy without global breakaway.

201 average at a fixed location). The LAVD is hence given by

$$LAVD_{t_0}^{t_1}(x_0, y_0) = \frac{1}{t_1 - t_0} \int_{t_0}^{t_1} |\zeta'[X(x_0, y_0, t), Y(x_0, y_0, t), t]| dt . \quad (7)$$

202 The LAVD is a function of position (x_0, y_0) but also depends on the time interval t_0, t_1 . RCLV
203 boundaries at time t_0 are then defined as the outermost convex and closed LAVD curves surround-
204 ing local maxima of the LAVD field. The maxima themselves are the Lagrangian vortex centers,
205 which can be proven to be attractors or repellors for floating debris, depending on the polarity of
206 the eddy (c.f. Haller et al. 2016). Details of the numerical computation of RCLVs are given in
207 Sec. 4.

208 Once the RCLVs are identified for a specific time interval, it is straightforward to compute the
209 associated contribution to dispersion and diffusivity. We define a masking function $m_{t_0}^{t_1}$ to be 1
210 inside each RCLV boundary and 0 outside. The *coherent relative diffusivity* is then defined as

$$K_{rel}^{cs} = \frac{1}{2} \frac{\partial}{\partial t} \overline{m_{t_0}^{t_1} (Y - \bar{Y})^2} . \quad (8)$$

211 The $m_{t_0}^{t_1}$ factor masks all regions that are not within a coherent structure, effectively assuming such
212 regions move only with the mean flow and induce no relative dispersion. By comparing K_{rel}^{cs} with
213 K_{rel} , we thereby quantify the fraction of meridonal eddy transport due to coherent structures. If
214 it is true that eddy transport is “mainly due to individual eddy movements” (Dong et al. 2014),
215 then $K_{rel}^{cs} \simeq K_{rel}$. In contrast, if most of the transport is due to *incoherent* motion outside of the
216 structures, then $K_{rel}^{cs} \ll K_{rel}$. Note that K_{rel}^{cs} includes two distinct modes of dispersion: coherent
217 meridional motion of the whole eddy and rotation of the water parcels within the eddy.

218 3. Satellite Data and Particle Advection

219 To identify RCLVs and compute relative dispersion, we use satellite-derived surface geostrophic
220 velocities to numerically advect virtual Lagrangian particles. In this study, we consider only trans-

port by the two-dimensional near-surface geostrophic velocity. This is of course an incomplete representation of the full flow field, but the geostrophic flow is by far the dominant component at the scales of interest here. It was shown by Rypina et al. (2012) that Ekman currents, the main large-scale ageostrophic motion in the open ocean, make a negligible contribution to mesoscale dispersion compared to the geostrophic flow. In the conclusions, we speculate about the possible role of ageostrophic and / or unresolved motion for the detection of RCLVs.

a. AVISO Surface Geostrophic Velocities

The surface geostrophic velocity field (\mathbf{v}_g) is related to the sea surface height (SSH) relative to the geoid (η) via

$$\hat{\mathbf{k}} \times \mathbf{v}_g = -\frac{g}{f} \nabla \eta \quad (9)$$

where f is the Coriolis parameter, g is the gravitational acceleration, and $\hat{\mathbf{k}}$ is the unit vector pointing out of the sea surface. Satellite altimetry measures the SSH η .

We employ pre-computed gridded geostrophic velocities from the AVISO. The AVISO gridding process uses objective interpolation (Barnes 1964, their terminology is unrelated to the objectivity of coherent structures) to map along-track satellite radar altimetry from various platforms onto a $1/4^\circ$ latitude-longitude grid (Ducet et al. 2000). In addition to providing pre-computed geostrophic velocities, this product also applies a higher-order vorticity balance to estimate velocities in the equatorial region (within $\pm 5^\circ$) where geostrophy does not hold (Lagerloef et al. 1999). While this provides a complete global surface velocity field, the results in this equatorial band are less reliable. The data were downloaded in 2015 and reflect the most recent AVISO algorithm and processing available at that time. We use the delayed-time, reference, all-satellite merged product.

We consider the time period from Jan. 1, 1993 - Oct. 17, 2014.

242 An additional processing step was undertaken: we applied a small correction to the AVISO
243 geostrophic velocity field to remove the divergence due to the meridional variation of f and
244 to enforce no-normal-flow boundary conditions at the coastlines. The resulting velocity field,
245 henceforth denoted simply v , is an exactly two-dimensional non-divergent flow. The correction
246 procedure is described in detail by Abernathey and Marshall (2013), who demonstrate that the
247 corrections are small in magnitude compared to the original geostrophic velocity. We compared
248 corrected vs. non-corrected LAVD fields and found a negligible impact on the identification of
249 RCLVs in the open ocean.

250 *b. Advection of Lagrangian Particles*

251 As noted by Haller et al. (2016), the *LAVD* field may contain structure on smaller scales than
252 the scales of the velocity field itself. This is related to the fact that a relatively coarse chaotic
253 advection field can produce very fine structure in passive tracers (Pierrehumbert 1991). Practically,
254 it means that an extremely dense mesh of Lagrangian particles is required to properly resolve
255 the *LAVD*. This leads to a significant computational burden if, as here, one wishes to study a
256 large geographical area and temporal extent. The AVISO product is gridded at $1/4^\circ$ resolution
257 and resolves SSH anomalies of roughly 50 km and larger (CSS11). However, sensitivity tests
258 indicated that an initial particle spacing of $1/32^\circ$ is necessary to achieve sufficient accuracy in the
259 LAVD field and identification of RCLVs. The mesh of initial positions is located between 180°
260 and 130° W longitude and 80° S and 80° N latitude, a total of 8192000 points. (In retrospect,
261 many of the high-latitude particles were not useful, since they lie within land points or within the
262 marginal sea-ice zone where AVISO velocities are not available. We restrict the analysis to the
263 latitude range 65° S - 60° N.)

264 The initial particle positions (at time t_0) determine the discrete coordinates of the *LAVD* field.
265 These initial positions can therefore be chosen to facilitate the identification of RCLVs. In particu-
266 lar, the first step in the algorithm requires the maxima of *LAVD* to be identified (Haller et al. 2016).
267 The most obvious initial deployment, a rectangular grid, is actually not ideal for the robust iden-
268 tification of maxima because the relationship between diagonally connected points is ambiguous;
269 a better choice is a hexagonal grid, in which each point has six unambiguous neighbors (Kuijper
270 2004). To transform a rectangular mesh to a hexagonal one, every other row is offset by $\Delta x/2$,
271 where $\Delta x = 1/32^\circ$ is the spacing in the zonal direction.

272 We seek to identify RCLVs with lifetimes of 30, 90, and 270 days. Accordingly, we segment
273 the time domain into non-overlapping N -day intervals (a total of 265 30-day, 88 90-day, and 29
274 270-day intervals). While the specific interval bounds are arbitrary, RCLVs are structurally stable
275 by construction, i.e. small changes in the extraction interval will have a small effect. If we identify
276 a RCLV over a given time interval, this structure will generally be a subset of a larger RCLV that
277 we would obtain in the same location for shorter time intervals. So we would not lose any of the
278 RCLVs if we picked shorter time intervals (unless we pick such short intervals that Lagrangian
279 coherence can no longer be established from the available data). Rotational coherence is a finite-
280 time notion and hence the same water mass may become incoherent over longer times. It is still
281 possible that we miss some short-lived RCLVs over longer time intervals.

282 The Lagrangian trajectories are determined by solving the equation $d\mathbf{X}/dt = \mathbf{v}$ numerically us-
283 ing the MITgcm (Adcroft et al. 2014), an ocean general circulation model. Although this model is
284 primarily designed for prognostic ocean simulations, it has several features that make it an attrac-
285 tive choice for computationally demanding Lagrangian simulations. First, it can operate in offline
286 mode, in which velocity fields are read from files. Second, it supports Lagrangian particle tracking
287 (via the `f1t` package) and implements fourth-order Runge-Kutta integration. Finally, MITgcm can

288 run efficiently in a massively parallel configuration on many nodes of a high-performance com-
289 puting cluster, providing the necessary memory and CPU performance to enable large Lagrangian
290 ensembles.

291 An MITgcm run was performed for each of the temporal segments described above, and particle
292 data was output daily. (Relative vorticity was calculated on the Eulerian grid and interpolated
293 bilinearly to particle positions.) The total data volume of output generated for the study was over
294 2 TB. The identification of RCLVs from this data is described in the following section.

295 **4. Identification and Statistics of Lagrangian Vortices**

296 *a. Algorithm*

297 The algorithm employed for identifying RCLVs follows Haller et al. (2016), with some slight
298 modifications for computational efficiency.

- 299 1. At time t_0 , initialize a hexagonal mesh of Lagrangian particles over the domain.
- 300 2. Advect particles forward until time $t_0 + T$, where T is the desired vortex lifetime (here 30, 90
301 and 270 days). Output particle position and relative vorticity every day.
- 302 3. Average the vorticity deviation (absolute value of relative vorticity minus global mean vortic-
303 ity) over particle trajectories and map back to initial positions x_0 . The resulting field is the
304 *LADV*.

- 305 4. Identify maxima of *LADV*. (Maxima are unambiguously identified on a hexagonal mesh.)
306 These are the RCLV centers.

- 307 5. Find the largest closed and convex curves around *LADV* maxima. These are the RCLV bound-
308 aries. The regions are grown iteratively by adding points; iteration stops when the next point

309 to be added lies within the convex hull of the current region. This method admits a small
310 convexity deficiency (usually of order 0.01) in the curves to account for the discrete nature of
311 the numerically computed LAVD field.

312 6. Filter the RCLVs by discarding features with area below a minimal admissible size (here
313 chosen to be the area of a circle with a diameter of 30 km)

314 This algorithm, as well as other general-purpose data processing routines for MITgcm par-
315 ticle trajectories, was implemented in a python package called floater, available at <https://github.com/rabernat/floater>. An example of the *LAVD* field, together with the positions
316 of identified RCLVs, is shown in Fig. 1.
317

318 *b. Example Vortices*

319 The initial and final locations of two randomly selected 90-day RCLVs are shown in Fig. 2,
320 superimposed on the SSH anomaly field. One is located in the North Pacific subtropical gyre,
321 while the other is in the Antarctic Circumpolar Current. These vortices clearly remain materially
322 coherent over the 90-day lifetime, consistent with the results of (Haller et al. 2016). We examined
323 hundreds of examples and found similar behavior. This should be contrasted to the behavior of
324 SSH eddies, whose boundaries are rapidly deformed under advection by the surface geostrophic
325 flow (Beron-Vera et al. 2013).

326 One noteworthy feature of these example RCLVs is that they do appear embedded within SSH
327 anomalies. However, the coherent core is much smaller than the SSH anomaly. Here we do not
328 attempt to comprehensively compare the RCLVs with tracked SSH eddies on a feature-by-feature
329 basis, but a statistical comparison (next subsection) suggests that this difference in size holds in
330 general.

331 c. Vortex Statistics

332 In this section we calculate some statistics of all the identified RCLVs and compare them to
333 the statistics of the tracked SSH eddies of CSS11, whose data is publicly available at <http://wombat.coas.oregonstate.edu/eddies/>. We identified 41875, 30-day RCLVs, 1182 90-day
334 RCLVs, and only 1 270-day RCLV in the period 1993-2015. The trajectories for all the 30-day
335 RCLVs are plotted in Fig. 3. The average number of RCLVs per degree of latitude per year is
336 plotted in Fig. 4. (270-day RCLVs are excluded from all subsequent discussion, since they are
337 almost non-existent.) Both figures reveal the densest concentration of RCLVs in midlatitudes,
338 with very few RCLVs detected in the tropics. This is broadly similar to SSH eddies.
339

340 The comparison of the occurrence of 30-day vs. 90-day RCLVs in Fig. 4 reveals that the shorter-
341 lived vortices are much more prevalent. There are actually more 30-day RCLVs than SSH eddies
342 with lifetimes larger than 30 days. However, the reverse is true for 90-day RCLVs; there are many
343 more SSH eddies with equivalent or longer lifetimes. The comparison with 270-day RCLVs,
344 which are essentially non-existent, is even more extreme; the census of CSS11 identifies 2076
345 SSH eddies with lifetimes at least that long.

346 We now examine the statistics of eddy size. The RCLV area A is converted to a radius r via
347 the formula $r = \sqrt{A/\pi}$. Most of the RCLVs are approximately circular (e.g. Fig. 2), and this
348 conversion yields a familiar unit for assessing length scales. In Fig. 5, we plot this radius and
349 compare it to the radius of SSH eddies from CSS11. Statistics are calculated in 5-degree latitude
350 bins.

351 Outside of the tropics (where RCLVs are rare), Fig. 5 reveals a familiar inverse relationship
352 between eddy size and latitude, which likely reflects the dependence of the Rossby deformation
353 radius on the Coriolis parameter (Chelton et al. 1998). The largest median RCLV radius occurs

354 near $\pm 30^\circ$, where it approaches 40 km. Comparing with CSS11, the median RCLV radius is
355 roughly about half of the median SSH eddy. This is consistent with the example vortices shown in
356 Fig. 2. The SSH size statistics diverge qualitatively from the RCLVs in the tropics.

357 In Fig. 6, we examine the zonal propagation speed of RCLVs and SSH eddies. In both cases, the
358 zonal propagation speed is calculated as the total zonal distance traveled over the eddy lifetime.
359 From this point of view, RCLVs and SSH eddies look very similar, with much faster propagation
360 at low latitudes due to the larger gradient in Coriolis parameter (i.e. β -effect; Chelton et al. 2011;
361 Klocker and Abernathey 2014; Abernathey and Wortham 2015). Again, the statistics diverge in
362 the topics, where there are vanishingly few RCLVs.

363 Since the RCLVs and SSH eddies propagate at the same speed, one might expect that the Eule-
364 rian methods of CSS11 and the Lagrangian method used here identify broadly similar structures.
365 However, the radius statistics suggest that the rotationally coherent core of mesoscale eddies is
366 considerably smaller (by half) than the radius inferred from by CSS11. Furthermore, there is a
367 significant difference in eddy lifetime; the SSH eddies last much longer than the RCLVs. This
368 might indicate that many SSH eddies represent materially leaky dynamical structures, which ex-
369 change water with their surroundings. While we have not conducted a comprehensive investigation
370 of RCLV lifetime, the fact that there were essentially zero 270-day RCLVs in the sector provides
371 an upper bound for the timescale of this leaky exchange. On the other hand, Wang et al. (2015)
372 found numerous materially coherent Agulhas eddies with 360-day lifetimes, suggesting that dif-
373 ferent regions of the ocean may generate less leaky eddies. This discrepancy may be addressed in
374 future work by applying the RCLV method at a global scale.

375 **5. Meridional Transport by Lagrangian Vortices**

376 Having described the method of identifying of coherent Lagrangian vortices, we now turn to
377 the central question of our study: the role of these RCLVs in material transport. For each 30
378 and 90-day interval, we compute the absolute diffusivity K (eq. 4) and relative diffusivity K_{rel}
379 (eq. 5) as a function of latitude using the full ensemble of Lagrangian particles. We also compute
380 the fractional relative diffusivity K_{rel}^{cs} (8), using only particles inside the RCLVs. As discussed in
381 Sec. 2, K_{rel}^{cs} represents the diffusivity which would result if water parcels outside of the RCLVs
382 moved only with the zonal mean flow and induced no relative dispersion.

383 The results of these diffusivity calculations are shown in Fig. 7. First, we note that there is
384 minimal difference between K and K_{rel} , revealing that there is negligible mean meridional advec-
385 tion throughout the sector. K_{rel} ranges from $500 - 6000 \text{ m}^2 \text{ s}^{-1}$, with highest values found in the
386 tropics. This is broadly consistent with previous estimates from this sector (Zhurbas and Oh 2003;
387 Abernathey and Marshall 2013; Klocker and Abernathey 2014; Abernathey and Wortham 2015).
388 Precise agreement with previous studies is not necessarily expected, since relative diffusivity de-
389 pends sensitively on the time interval (Okubo 1971; Ollitrault et al. 2005; LaCasce 2008). For
390 homogeneous flows, convergence is expected for long time scales (Klocker et al. 2012), but the
391 diffusivities here correspond precisely to 30- and 90-day time intervals. The difference between
392 the 30- and 90-day results show that convergence has not been reached everywhere.

393 The emphasis here is not the precise value of K_{rel} but rather the comparison with K_{rel}^{cs} (middle
394 panel). The most striking difference is the order of magnitude: K_{rel}^{cs} does not exceed $10 \text{ m}^2 \text{ s}^{-1}$
395 for 30-day RCLVs and does not exceed $1 \text{ m}^2 \text{ s}^{-1}$ for 90-day RCLVs. We can quantify the fraction
396 of transport accomplished by RCLVs at each latitude via the ratio $R_K = K_{rel}^{cs}/K_{rel}$, as plotted in
397 in Fig. 7 (bottom panel). This fraction would be close to one if most of the transport were by

398 coherent vortices; instead, we observe that it never exceeds 0.005 for 30-day RCLVS and is an or-
399 der of magnitude smaller for 90-day RCLVS. This small contribution of RCLVs to the meridional
400 transport mirrors the finding of Wang et al. (2015) that materially coherent Agulhas eddies make
401 a very small contribution to net transport in that region—we return to this point in the discussion.

402 The similarity between the shape of K_{rel}^{cs} and the average density of RCVLs (Fig. 4) suggests that
403 the primary control on K_{rel}^{cs} is simply the density of RCLVs found at a particular latitude. To test
404 this hypothesis, we compute the RCLV area fraction R_A (Fig. 7, bottom panel), which represents
405 the average fraction of the ocean surface area that lies within an RCLV in each latitude band.
406 For 30-day RCLVs, R_A peaks at around 0.025 and is an order of magnitude smaller for 90-day
407 RCLVs. This is significantly higher than R_K , the diffusivity fraction, revealing that the RCLVs
408 are actually regions of anomalously *low* meridional dispersion. This is unsurprising, since the
409 RCLVs remain coherent by construction and undergo relatively low filamentation compared to the
410 background flow. In other words, randomly selected patches of ocean with the same surface area
411 as the identified RCLVs would experience stronger meridional diffusion than the actual RCLVs.

412 **6. Discussion and Conclusion**

413 Many prior studies have attempted to track mesoscale eddies by following anomalies in the SSH
414 field (and associated instantaneous surface geostrophic velocity field) through time (e.g. Chelton
415 et al. 2011; Dong et al. 2011; Faghmous et al. 2015). While such tracked Eulerian eddies may
416 be useful for some applications, the work of Beron-Vera et al. (2013) and Haller and Beron-
417 Vera (2013) has shown that structures identified in this way are not generally materially coherent:
418 significant material leakage can occur through the supposed structure boundaries. This finding
419 calls into question studies such as those of Dong et al. (2014) and Zhang et al. (2014), who attempt
420 to infer heat, salt, and mass transports based on the displacement of tracked Eulerian eddies. The

421 goal of our study was to examine the material transport of mesoscale eddies defined as Lagrangian
422 Coherent Structures.

423 We identified coherent eddies across a broad sector in the Eastern Pacific using an objective,
424 Lagrangian method based on the vorticity, the so-called Rotationally Coherent Lagrangian Vortex
425 (RCLV) approach of Haller et al. (2016). This computationally demanding task required the nu-
426 merical advection of millions of virtual Lagrangian particles over a period of 25 years, the length
427 of the satellite altimetry record. To our knowledge, our study is the largest-scale application of
428 objective Lagrangian eddy detection to date. This comprehensive census of RCLVs in the sector
429 allowed us to a) calculate some statistical properties of RCLVs and b) compute their contribution
430 to net meridional transport, via a the coherent relative diffusivity K_{rel}^{cs} .

431 The occurrence frequency, length scales, and propagation speeds of RCLVs in this sector were
432 found to be qualitatively similar to those of SSH eddies identified by Chelton et al. (2011). RCLVs
433 were larger at low latitude, consistent with the meridional variations in the baroclinic Rossby
434 deformation radius; the RCLV radii, however, were smaller than the SSH eddy radii by about a
435 factor of two. A more striking difference was the eddy lifetime; while we didn't systematically
436 examine the dependence on the extraction interval, we found essentially no RCLVs with lifetimes
437 longer than 270 days. We suggested that this sets an upper bound on the leakiness timescale of
438 mesoscale eddies in this sector. The comparison between RCLVs and SSH eddies raises many
439 further questions about the relationship between the different methods. How often are RCLVs
440 embedded inside SSH eddies? Is it possible to quantify the leakiness of the SSH eddies? Is the
441 Eulerian nonlinearity parameter U/c (with u the azimuthal eddy velocity and c the translation
442 speed) of Chelton et al. (2011) related to the presence of RCLVs? These questions are ripe for
443 exploration in future work.

444 Our primary focus here has been the calculation of meridional transport by RCLVs. Our key
445 finding is that K_{rel}^{cs} , representing the diffusive meridional transport due to RCLVs, is hundreds of
446 times smaller than K_{rel} , the diffusive meridional transport of the full flow. This means means that
447 transport by RCLVs makes a negligible contribution to the net meridional dispersion. By process
448 of elimination, we can then conclude that, in this sector, meridional dispersion is primarily by
449 *incoherent* motions, outside of the RCLV boundaries. This conclusion is in contradiction with
450 the claims of Dong et al. (2014) and Zhang et al. (2014), who base their transport estimates on
451 Eulerian eddy tracking. Our conclusion *is*, however, highly consistent with the findings of Wang
452 et al. (2015), who used a different objective Lagrangian eddy identification method to quantify
453 material transport by Agulhas rings. Indeed, Wang et al. (2015) found that the cross-Atlantic
454 transport by materially coherent Agulhas eddies was two orders of magnitude smaller than prior
455 estimates based on Eulerian eddy tracking. Since Agulhas rings move only in one direction, Wang
456 et al. (2015) described the transport in terms of advection. In our sector, where eddies drift both
457 north and south with equal frequency, transport was quantified in terms of diffusion. (A more
458 general statistical decomposition of transport by coherent Lagrangian eddies would involve both
459 advection and diffusion.) Regardless, the overall conceptual agreement between their study and
460 ours, which used a different method and examined a different region, suggests that relatively small
461 material transport by coherent Lagrangian eddies is a robust result.

462 This finding does not mean, however, that coherent mesoscale eddies are insignificant for trans-
463 port. Indeed, studies in the spectral domain (e.g. Killworth et al. 2004; Abernathey and Wortham
464 2015) show that the eddy flux peaks at length scales and phase speeds associated with mesoscale
465 eddies. Our results here, however, suggest that the meridional eddy transport is likely driven by
466 stirring and filamentation on the periphery of coherent eddies, rather than by coherent meridional
467 motion of the eddy core. This mechanism was illustrated clearly by Hausmann and Czaja (2012),

468 who studied eddy heat transport by examining the cross-correlation structure between satellite-
469 observed SSH and SST anomalies. Using the cross-correlation, they decomposed the Eulerian
470 eddy heat flux into a drift component (associated with translation of fluid within the eddy core)
471 and a swirl component, associated with peripheral stirring. They found that the swirl component
472 was large enough to make a leading-order contribution to the oceanic heat budget, but that the drift
473 component was negligible. This finding is compatible with our results, but not with Dong et al.
474 (2014), who reached the opposite conclusion through methods similar to Hausmann and Czaja
475 (2012).

476 The chief limitation of the results we have presented is their reliance on the AVISO surface
477 geostrophic velocities, which we have simply accepted at face value as adequately representative
478 of the near-surface flow. In reality, there are many potential sources of error in these velocity fields
479 including measurement error of the altimeter itself, limited spatial and temporal sampling, map-
480 ping errors related to the gridding of satellite tracks, and the presence of ageostrophic and vertical
481 velocities. Lagrangian coherent structures represent stable attractors of the flow and are robust to
482 the presence of small noise (Haller 2015). The spatial and temporal sampling issue, however, is
483 likely more serious; Keating et al. (2012) showed that such subsampling can seriously degrade the
484 finite-time Lyapunov exponent field in idealized turbulence simulations. It is an open question how
485 the presence of submesoscale flows and internal waves impacts the leakiness of mesoscale trans-
486 port barriers and eddies. A comprehensive investigation of the observational errors in the detection
487 of Lagrangian coherent structures from satellite altimetry observations would indeed be a valuable
488 contribution. The full three-dimensional structure of RCLVs also remains an open question which
489 is not possibly to address using satellite observations alone. Analysis of a high-resolution general
490 circulation model would be a good way to probe this question.

491 We see this study as the first step towards a fully global characterization of mesoscale coherent
492 structures. It is our hope that this sort of detailed description of the Lagrangian kinematics of
493 mesoscale transport will eventually lead to more accurate parameterization of mesoscale transport
494 in coarse-resolution climate models. In the case of the Eastern Pacific, it appears that we can
495 reliably neglect long-range meridional transport due to fluid trapping within coherent eddy cores.
496 This is good news from the perspective of parameterization, since the swirling mode of eddy
497 transport seems more amenable to representation via diffusive closures. Determining whether such
498 a conclusion holds more generally will have to await the completion of a global-scale Lagrangian
499 eddy census, which is a serious computational challenge.

500 *Acknowledgments.* R.P.A. gratefully acknowledges the support of an NSF CAREER award (OCE
501 1553593). We thank Nathaniel Tarshish, Ivy Frenger, Carolina DuFour, and Steve Griffies for their
502 feedback on this manuscript.

503 References

- 504 Abernathey, R., and J. C. Marshall, 2013: Global surface eddy diffusivities derived from satellite
505 altimetry. *J. Geophys. Res.*, **118**, 901–916, doi:10.1002/jgrc.20066.
- 506 Abernathey, R. P., and C. Wortham, 2015: Phase speed cross spectra of eddy heat fluxes in the
507 pacific. *J. Phys. Oceanogr.*, **45**, 1285–1301, doi:10.1175/JPO-D-14-0160.1.
- 508 Adcroft, A., and Coauthors, 2014: MITgcm user manual. MIT Department of EAPS Cambridge,
509 URL http://mitgcm.org/public/r2_manual/latest/online_documents/manual.html.
- 510 Bachman, S., and B. Fox-Kemper, 2013: Eddy parameterization challenge suite i: Eady spindown.
511 *Ocean Modelling*, **64**, 12–18.

- 512 Barnes, S. L., 1964: A technique for maximizing details in numerical weather map analysis.
- 513 *Journal of Applied Meteorology*, **3** (4), 396–409.
- 514 Batchelor, G., 1952: The effect of homogeneous turbulence on material lines and surfaces. *Proceedings of the Royal Society of London A: Mathematical, Physical and Engineering Sciences*,
- 515 The Royal Society, Vol. 213, 349–366.
- 516 Bennett, A. F., 1984: Relative dispersion: Local and nonlocal dynamics. *J. Atmos. Sci.*, **41**, 1881–1886.
- 517 Beron-Vera, F. J., Y. Wang, M. J. Olascoaga, G. J. Goni, and G. Haller, 2013: Objective detection
- 518 of oceanic eddies and the agulhas leakage. *Journal of Physical Oceanography*, **43** (7), 1426–1438.
- 519 Chelton, D. B., R. A. de Szoeke, M. G. Schlax, K. Naggar, and N. Siwertz, 1998: Geographical
- 520 variability of the first baroclinic rossby radius of deformations. *J. Phys. Oceanogr.*, **28**, 433–450.
- 521 Chelton, D. B., M. G. Schlax, and R. M. Samelson, 2011: Global observations of nonlinear
- 522 mesoscale eddies. *Progress in Oceanography*, **91**, 167–216.
- 523 Dong, C., J. C. McWilliams, Y. Liu, and D. Chen, 2014: Global heat and salt transports by eddy
- 524 movement. *Nature Comm.*, **5** (3294).
- 525 Dong, C., F. Nencioli, Y. Liu, and J. C. McWilliams, 2011: An automated approach to detect
- 526 oceanic eddies from satellite remotely sensed sea surface temperature data. *IEEE Geoscience*
- 527 and *Remote Sensing Letters*, **8** (6), 1055–1059, doi:10.1109/lgrs.2011.2155029.
- 528 Ducet, N., P. Y. Le Traon, and G. Reverdin, 2000: Global high-resolution mapping of ocean
- 529 circulation from TOPEX/Poseidon and ERS-1 and -2. *J. Geophys. Res.*, **105** (CH), 19,477–
- 530 19,498.

- 534 Faghmous, J. H., I. Frenger, Y. Yao, R. Warmka, A. Lindell, and V. Kumar, 2015: A daily
535 global mesoscale ocean eddy dataset from satellite altimetry. *Scientific Data*, **2**, Article num-
536 ber: 150 028.
- 537 Fox-Kemper, B., R. Lumpkin, and F. O. Bryan, 2012: Lateral transport in the ocean interior. *Ocean*
538 *Circulation and Climate – Observing and Modelling the Global Ocean*, G. Siedler, J. Church,
539 J. Gould, and S. Griffies, Eds., Elsevier.
- 540 Gent, P., J. Willebrand, T. McDougal, and J. McWilliams, 1995: Parameterizing eddy-induced
541 tracer transports in ocean circulation models. *J. Phys. Oceanogr.*, **25**, 463–475.
- 542 Haller, G., 2015: Lagrangian coherent structures. *Annual Review of Fluid Mechanics*, **47**, 137–
543 162.
- 544 Haller, G., 2016: Dynamic rotation and stretch tensors from a dynamic polar decomposition.
545 *Journal of the Mechanics and Physics of Solids*, **86**, 70–93.
- 546 Haller, G., and F. J. Beron-Vera, 2012: Geodesic theory of transport barriers in two-dimensional
547 flows. *Physica D: Nonlinear Phenomena*, **241** (20), 1680–1702, doi:10.1016/j.physd.2012.06.
548 012, URL <http://dx.doi.org/10.1016/j.physd.2012.06.012>.
- 549 Haller, G., and F. J. Beron-Vera, 2013: Coherent lagrangian vortices: The black holes of turbu-
550 lence. *Journal of Fluid Mechanics*, **731**, R4, doi:10.1017/jfm.2013.391.
- 551 Haller, G., A. Hadjighasem, M. Farazmand, and F. Huhn, 2016: Defining coherent vortices objec-
552 tively from the vorticity. *Journal of Fluid Mechanics*, **795**, 136–173.
- 553 Hausmann, U., and A. Czaja, 2012: The observed signature of mesoscale eddies in sea surface
554 temperature and the associated heat transport. *Deep Sea Res. I*, **70**, 60–72.

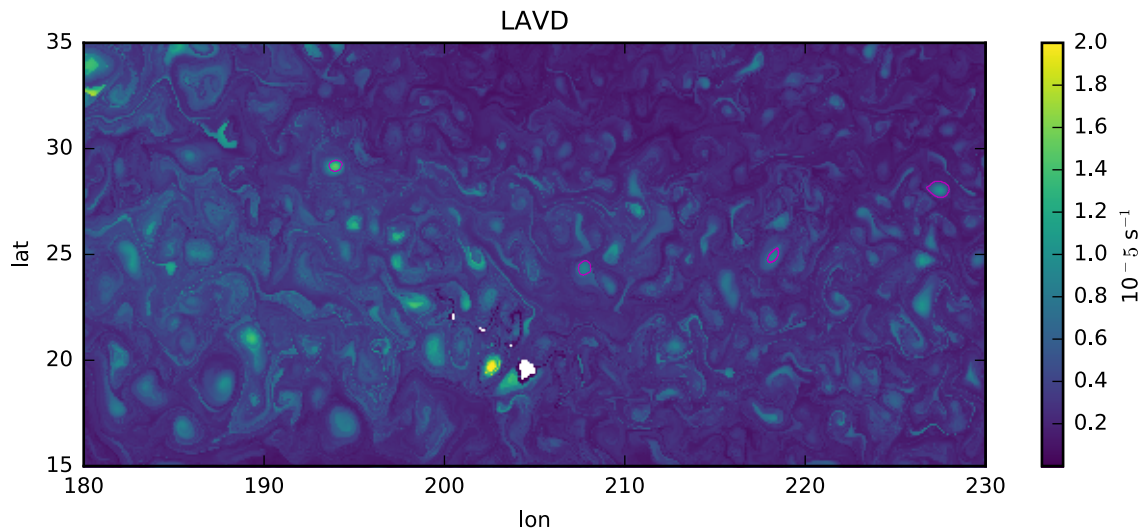
- 555 Isern-Fontanet, J., J. Font, E. García-Ladona, M. Emelianov, C. Millot, and I. Taupier-Letage,
556 2004: Spatial structure of anticyclonic eddies in the algerian basin (mediterranean sea) analyzed
557 using the okubo–weiss parameter. *Deep Sea Research Part II: Topical Studies in Oceanography*,
558 **51** (25), 3009–3028.
- 559 Isern-Fontanet, J., E. García-Ladona, and J. Font, 2003: Identification of marine eddies from
560 altimetric maps. *Journal of Atmospheric and Oceanic Technology*, **20** (5), 772–778.
- 561 Jayne, S. R., and J. Marotzke, 2002: The oceanic eddy heat transport. *J. Phys. Oceanogr.*, **32**,
562 3328–3345.
- 563 Keating, S. R., A. J. Majda, and K. S. Smith, 2012: New methods for estimating ocean eddy heat
564 transport using satellite altimetry. *Mon. Weather Rev.*
- 565 Killworth, P. D., P. Cipollini, B. M. Uz, and J. R. Blundell, 2004: Physical and biological mech-
566 anisms for planetary waves observed in satellite-derived chlorophyll. *J. Geophys. Res.*, **109**,
567 C07 002.
- 568 Klocker, A., and R. Abernathey, 2014: Global patterns of mesoscale eddy properties and diffusiv-
569 ities. *J. Phys. Oceanogr.*, **44**, 1030–1047, doi:10.1175/JPO-D-13-0159.1.
- 570 Klocker, A., R. Ferrari, J. H. LaCasce, and S. T. Merrifield, 2012: Reconciling float-based and
571 tracer-based estimates of eddy diffusivities. *J. Marine Res.*, **70** (4), 569–602.
- 572 Kuijper, A., 2004: On detecting all saddle points in 2d images. *Pattern Recognition Letters*,
573 **25** (15), 1665–1672, doi:10.1016/j.patrec.2004.06.017.
- 574 LaCasce, J. H., 2008: Statistics from lagrangian observations. *Progress in Oceanography*, **77**,
575 1–29.

- 576 Lagerloef, G., G. Mitchum, R. Lukas, and P. Niiler, 1999: Tropical Pacific near-surface currents
577 estimated from altimeter, wind and drifter data. *J. Geophys. Res.*, **104**, 313–23.
- 578 Morrow, R., J. Church, R. Coleman, D. Chelton, and N. White, 1992: Eddy momentum flux and
579 its contribution to the Southern Ocean momentum balance. *Nature*, **357**, 482–485.
- 580 Okubo, A., 1970: Horizontal dispersion of floatable particles in the vicinity of velocity singulari-
581 ties such as convergences. *Deep Sea Research and Oceanographic Abstracts*, **17 (3)**, 445–454.
- 582 Okubo, A., 1971: Oceanic diffusion diagrams. *Deep Sea Res.*, **18**, 789–802.
- 583 Ollitrault, M., C. Gabet, and A. C. De Verdiere, 2005: Open ocean regimes of relative dispersion.
584 *Journal of fluid mechanics*, **533**, 381–407.
- 585 Peacock, T., G. Froyland, and G. Haller, 2015: Introduction to focus issue: Objective detection of
586 coherent structures. *Chaos*, **25**, doi:10.1063/1.4928894.
- 587 Pierrehumbert, R. T., 1991: Chaotic mixing of a tracer and vorticity by modulated traveling rossby
588 waves. *Geo. Astro. Fluid Dyn.*, **58**, 285–320.
- 589 Roemmich, D., and J. Gilson, 2001: ddy transport of heat and thermocline waters in the North
590 Pacific: a key to interannual/decadal climate variability? *J. Phys. Oceanogr.*, **31**, 675–687.
- 591 Rypina, I. I., I. Kamenkovich, P. Berloff, and L. Pratt, 2012: Eddy-induced particle dispersion in
592 the near-surface atlantic. *J. Phys. Oceanogr.*, **42**, 2206–2228.
- 593 Serra, M., and G. Haller, 2017: Efficient computation of null geodesics with applications to co-
594 herent vortex detection. *Proc. R. Soc. A*, The Royal Society, Vol. 473, 20160807.
- 595 Stammer, D., 1998: On eddy characteristics, eddy transports, and mean flow properties. *J. Phys.*
596 *Oceanogr.*, **28**, 727–739.

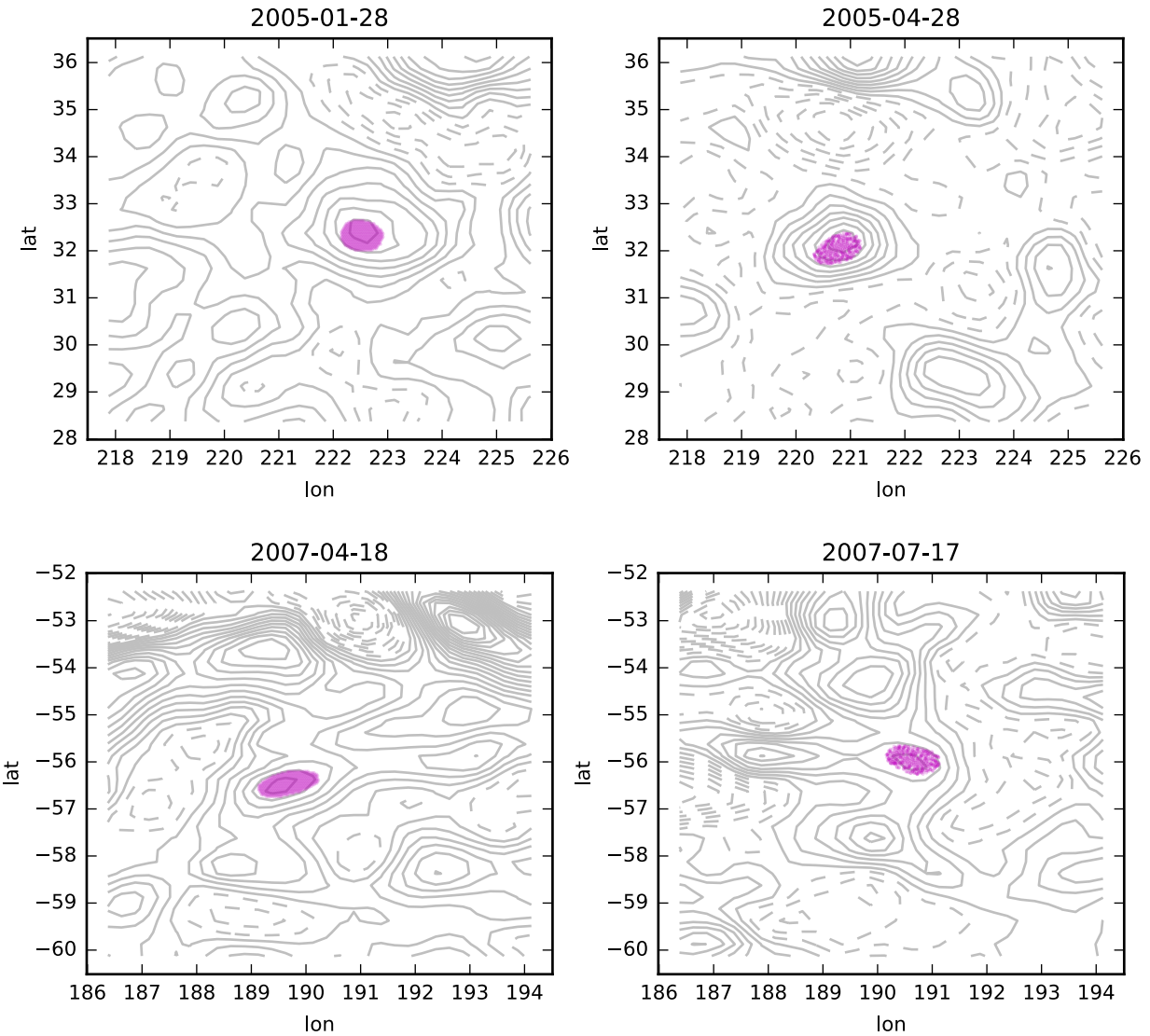
- 597 Taylor, G. I., 1921: Diffusion by continuous movements. *Proc . London Math. Soc.*, **s2-20**, 196–
598 212.
- 599 Treguier, A. M., I. Held, and V. Larichev, 1997: Parameterization of quasigeostrophic eddies in
600 primitive equation ocean models. *J. Phys. Oceanogr.*, **27**, 567–580.
- 601 Visbeck, M., J. Marshall, and T. Haine, 1997: Specification of eddy transfer coefficients in coarse-
602 resolution ocean circulation models. *J. Phys. Oceanogr.*, **27**, 381–403.
- 603 Volkov, D., T. Lee, and L. Fu, 2008: Eddy-induced meridional heat transport in the ocean. *Geo-
604 phys. Res. Lett.*, **35**, L20 601.
- 605 Vollmer, L., and C. Eden, 2013: A global map of mesoscale eddy diffusivities based on linear
606 stability analysis. *Ocean Modelling*, **72**, 198–209.
- 607 Wang, Y., M. J. Olascoaga, and F. J. Beron-Vera, 2015: Coherent water transport across the south
608 atlantic. *Geophysical Research Letters*, **42 (10)**, 4072–4079, doi:10.1002/2015GL064089.
- 609 Weiss, J., 1991: The dynamics of enstrophy transfer in two-dimensional hydrodynamics. *Physica
610 D: Nonlinear Phenomena*, **48 (2)**, 273–294.
- 611 Wortham, C., and C. Wunsch, 2014: A multidimensional spectral description of ocean variability.
612 *J. Phys. Oceanogr.*, **44**, 944–966.
- 613 Zhang, Z., W. Wang, and B. Qiu, 2014: Oceanic mass transport by mesoscale eddies. *Science*,
614 **345**, 322–324, doi:10.1126/science.1252418.
- 615 Zhurbas, V., and I. S. Oh, 2003: Lateral diffusivity and lagrangian scales in the Pacific ocean as
616 derived from drifter data. *J. Geophys. Res.*, **108 (C5)**, 3141.

617 LIST OF FIGURES

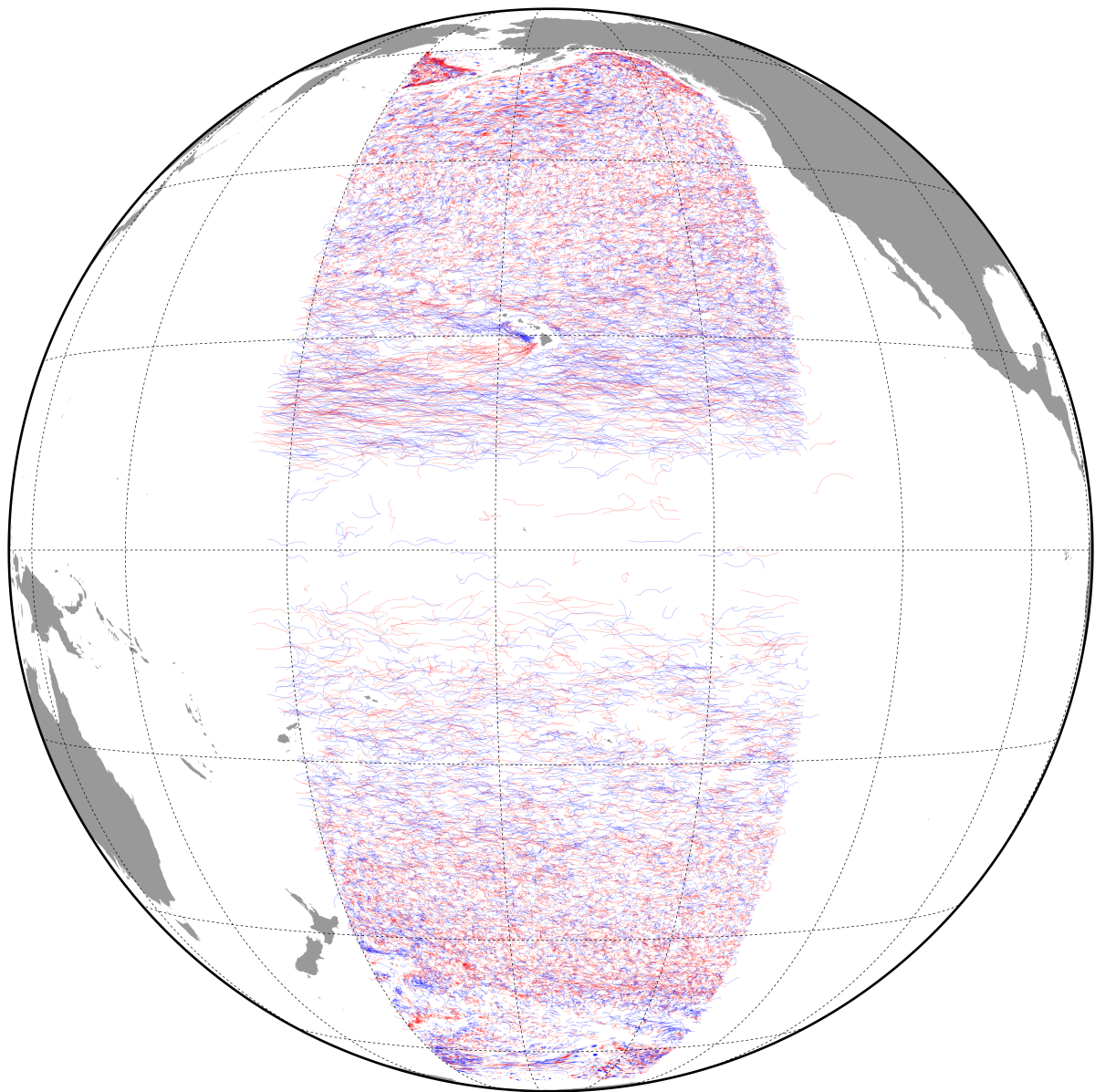
618	Fig. 1. A close-up example of a 90-day LAVD field from the region near Hawaii. Identified RCLV	31
619	boundaries are shown as magenta contours. Note that the large local LAVD maximum just	
620	west of Hawaii is not associated with an RCLV because the LAVD field near the maximum	
621	exhibits a spiraling filamentary structure. (This is indicative of vortex breakup during the	
622	interval.)	
623	Fig. 2. The initial (left) and final (right) locations of two randomly selected 90-day RCLVs. The	32
624	points contained within each RCLV boundary are visualized as magenta dots, overlaid on	
625	the contours of SSH anomaly. The contour interval for SSH is 2 cm.	
626	Fig. 3. The trajectories of the center points of all 46486 30-day RCLVs identified in the period	33
627	1993-2015. Trajectories represent actual Lagrangian water parcel paths under advection	
628	by the surface geostrophic flow. Cyclonic vortices are shown in blue and anticyclonic are	
629	shown in red.	
630	Fig. 4. Number of eddies per year per degree latitude in the east Pacific sector for RCLVs (this	34
631	study; solid line) and SSH eddies (Chelton et al. 2011, ; dashed line). The colors correspond	
632	to the eddy lifetime; black shows lifetimes of ≥ 30 days and red shows lifetimes of ≥ 90	
633	days.	
634	Fig. 5. Radius statistics of 30-day RCLVs (upper) and all SSH eddies (lower). Statistics of all eddies	35
635	in 5-degree bins are shown using a box-and-whisker plot. The red line indicates the median.	
636	The blue box spans the middle two quartiles (25th–75th percentiles) of the distribution. The	
637	black whiskers span the 10th–90th percentiles. Outliers are shown using the black + symbol.	
638	Fig. 6. As in Fig. 5, but for eddy zonal propagation speed.	36
639	Fig. 7. Upper panel: full relative diffusivity K_{rel} (5) averaged for all 30- (blue) and 90-day (green)	37
640	intervals. Middle panel: fractional relatively diffusivity K_{rel}^{cs} due only to the motion of	
641	RCLVs. Note the different scale on the y-axis. Bottom panel: non-dimensional ratios of	
642	RCLV area (R_A) and diffusivity (R_K) to total area and diffusivity.	



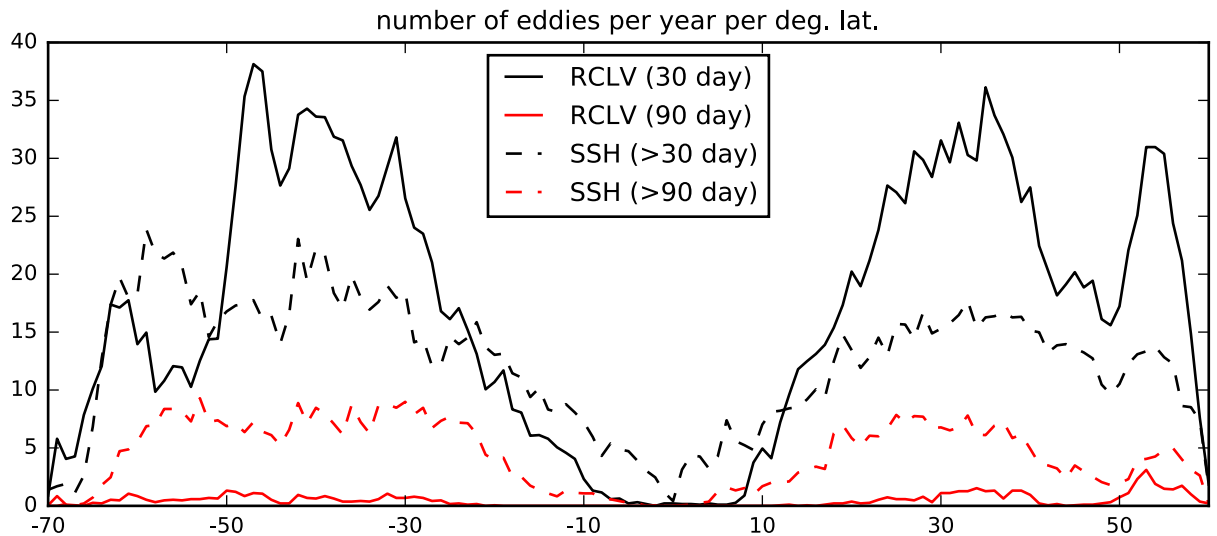
643 FIG. 1. A close-up example of a 90-day LAVD field from the region near Hawaii. Identified RCLV boundaries
 644 are shown as magenta contours. Note that the large local LAVD maximum just west of Hawaii is not associated
 645 with an RCLV because the LAVD field near the maximum exhibits a spiraling filamentary structure. (This is
 646 indicative of vortex breakup during the interval.)



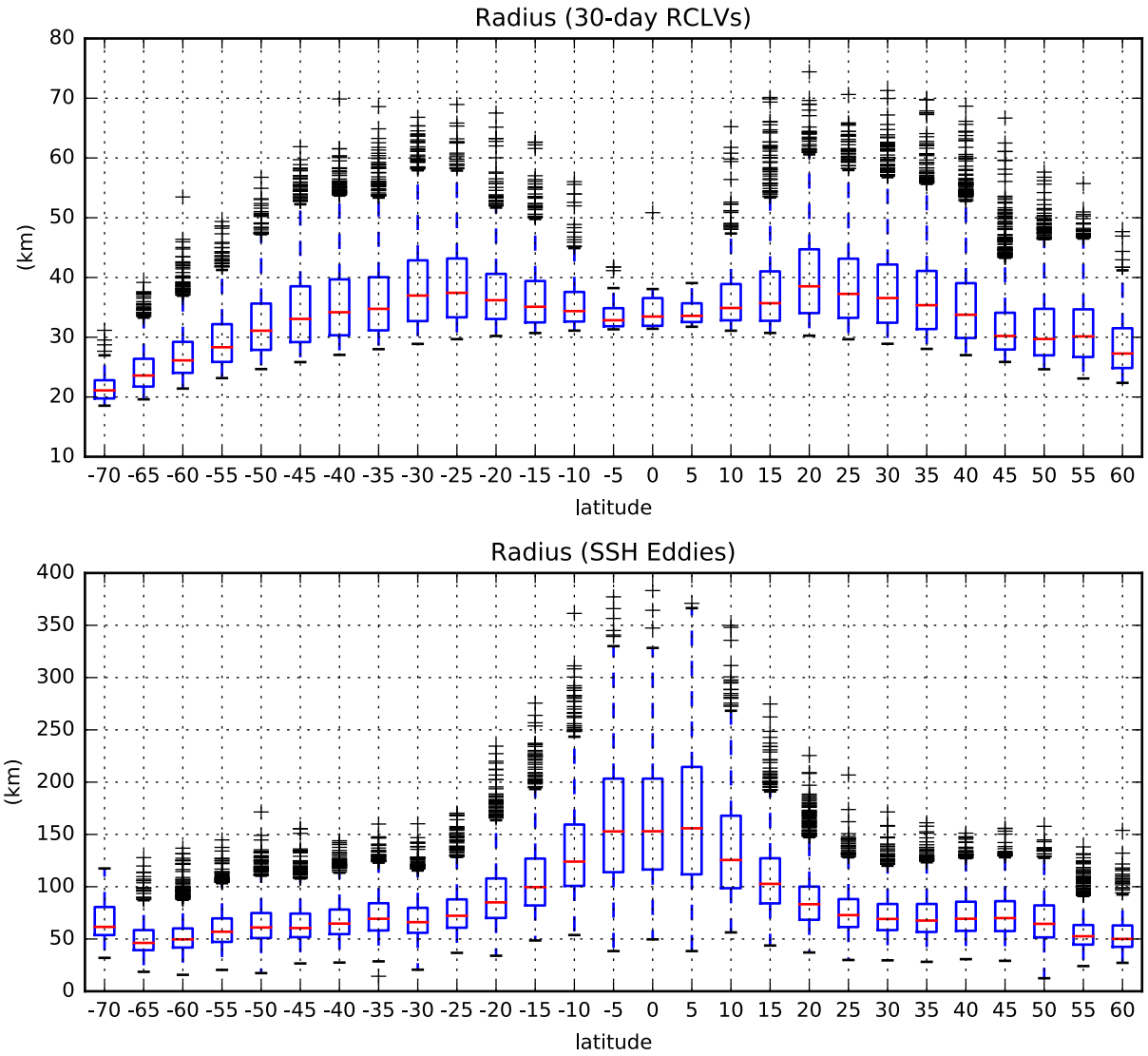
647 FIG. 2. The initial (left) and final (right) locations of two randomly selected 90-day RCLVs. The points
 648 contained within each RCLV boundary are visualized as magenta dots, overlaid on the contours of SSH anomaly.
 649 The contour interval for SSH is 2 cm.



650 FIG. 3. The trajectories of the center points of all 46486 30-day RCLVs identified in the period 1993-2015.
651 Trajectories represent actual Lagrangian water parcel paths under advection by the surface geostrophic flow.
652 Cyclonic vortices are shown in blue and anticyclonic are shown in red.



653 FIG. 4. Number of eddies per year per degree latitude in the east Pacific sector for RCLVs (this study; solid
 654 line) and SSH eddies (Chelton et al. 2011, ; dashed line). The colors correspond to the eddy lifetime; black
 655 shows lifetimes of ≥ 30 days and red shows lifetimes of ≥ 90 days.



656 FIG. 5. Radius statistics of 30-day RCLVs (upper) and all SSH eddies (lower). Statistics of all eddies in
 657 5-degree bins are shown using a box-and-whisker plot. The red line indicates the median. The blue box spans
 658 the middle two quartiles (25th–75th percentiles) of the distribution. The black whiskers span the 10th–90th
 659 percentiles. Outliers are shown using the black + symbol.

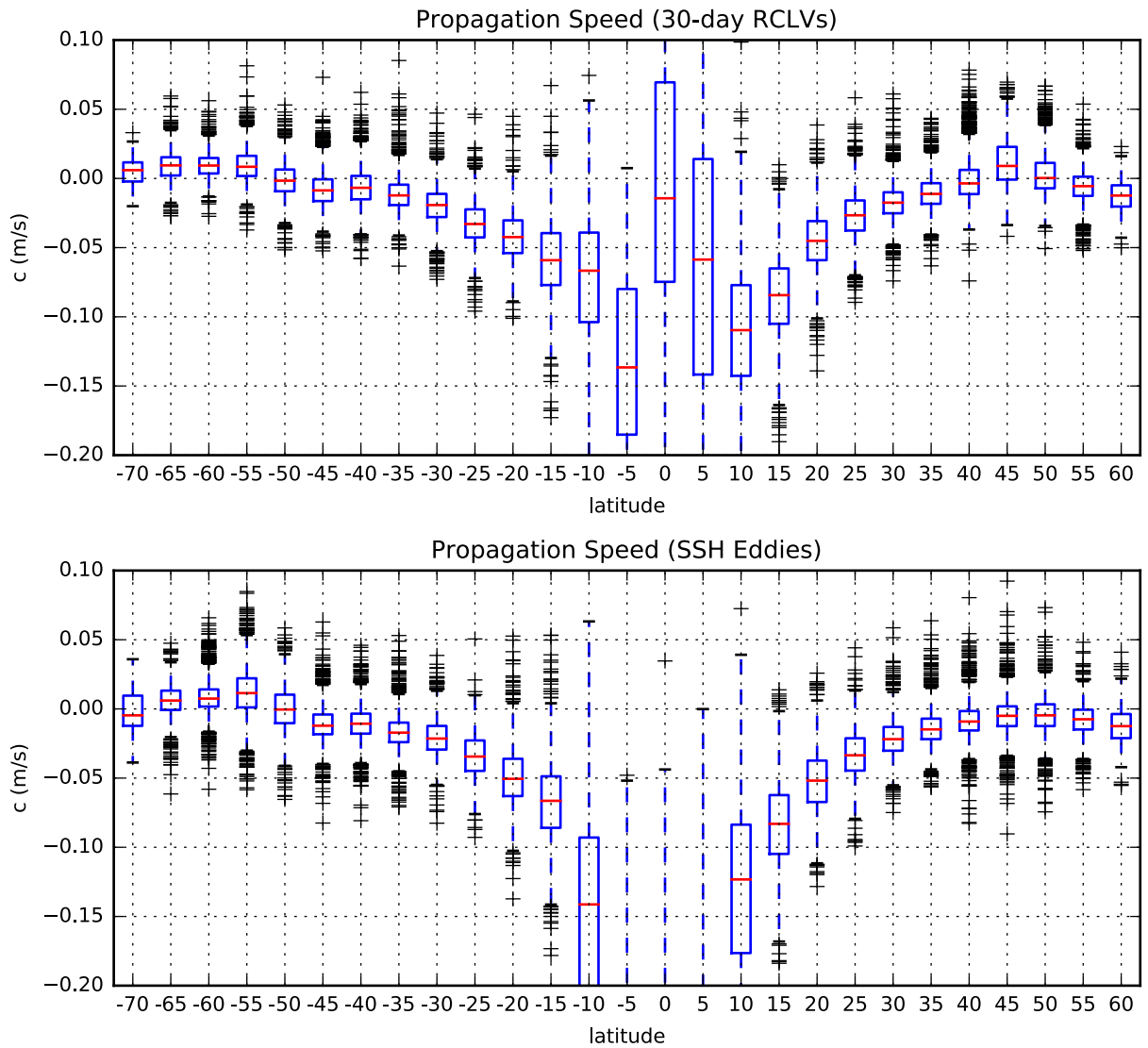
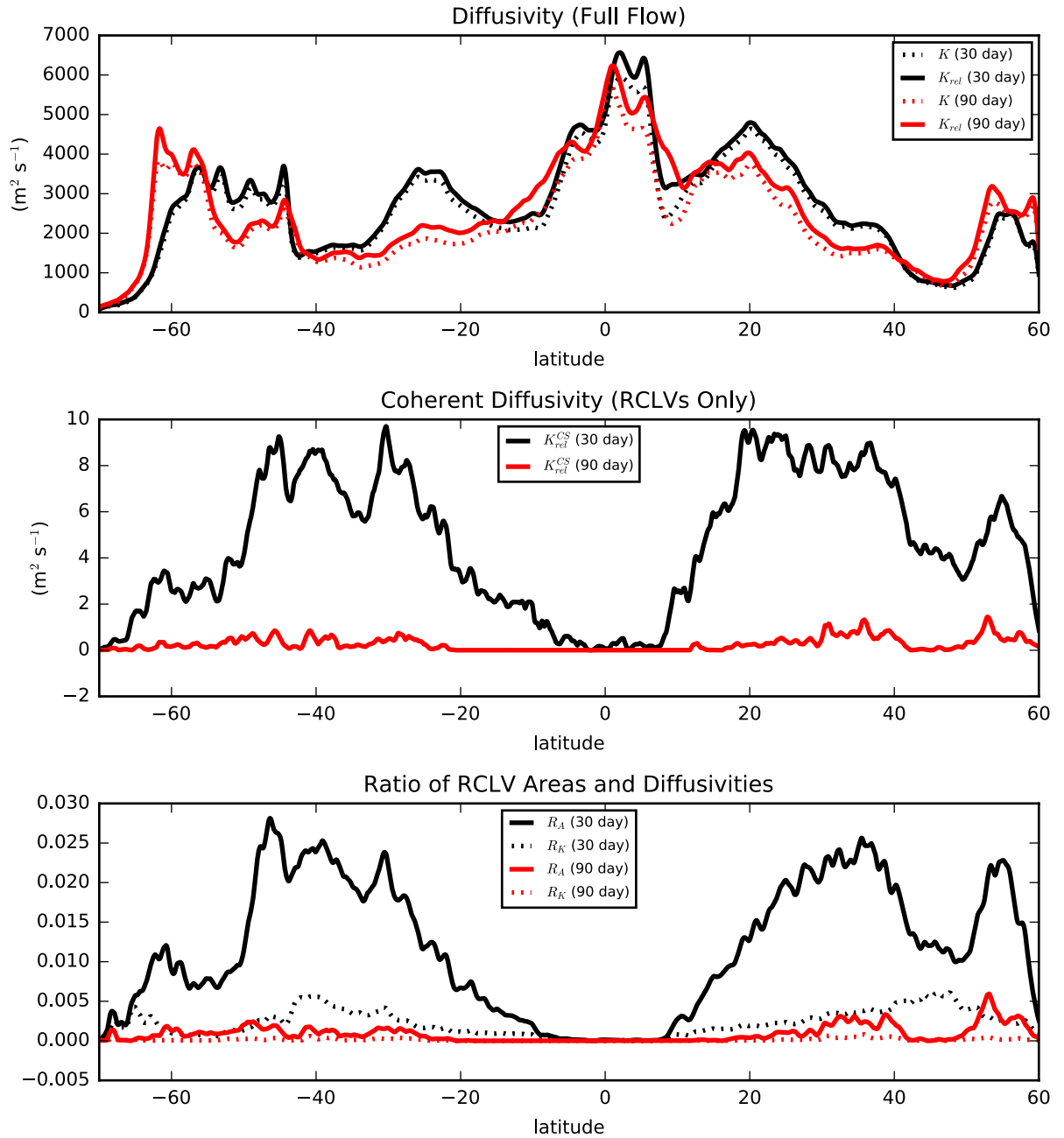


FIG. 6. As in Fig. 5, but for eddy zonal propagation speed.



660 FIG. 7. Upper panel: full relative diffusivity K_{rel} (5) averaged for all 30- (blue) and 90-day (green) intervals.
 661 Middle panel: fractional relatively diffusivity $K_{\text{rel}}^{\text{CS}}$ due only to the motion of RCLVs. Note the different scale
 662 on the y-axis. Bottom panel: non-dimensional ratios of RCLV area (R_A) and diffusivity (R_K) to total area and
 663 diffusivity.